

Article

Wind-Resistant Capacity Modeling for Electric Transmission Line Towers Using Kriging Surrogates and Its Application to Structural Fragility

Yunzhu Cai ^{1,*} and Jiawei Wan ^{2,*}

¹ College of Civil Engineering, Nanjing Tech University, No. 30 South Puzhu Road, Jiangbei New District, Nanjing 211816, China

² State Environmental Protection Key Laboratory of Atmospheric Physical Modeling and Pollution Control, State Power Environmental Protection Research Institute, No. 10 Pudong Road, Pukou District, Nanjing 210031, China

* Correspondence: yunzhucai@njtech.edu.cn (Y.C.); jiawei.wan@outlook.com (J.W.)

Featured Application: By applying the wind-resistant capacity model of transmission towers proposed in the article, it is capable to generate structural fragility curves for the tower, in which geo-spatial information of transmission line and wind (i.e., the line direction, the line span, and the wind direction) is considered simultaneously. Using the generated structural fragility model, the wind fragility assessment on transmission towers and line can be accomplished.

Abstract: Wind loading on a transmission tower structure is jointly influenced by the wind field, structural parameters, and the geo-spatial configuration of the transmission line. Considering the multi-parametric effect, this paper aims at developing a limit capacity model for transmission towers under strong winds. To this end, the limit capacity of the tower is expressed via two equivalent means: one is the limit wind speed as a function of the wind angle of attack and the span of transmission line; the other is a limit capacity surface with three fundamental wind load components as the principal axes. An adaptive kriging surrogate modeling is constructed to approximate the function/surface with structural uncertainties considered. The performance of the surrogate model is improved by adding support points and then evaluated by the overall accuracy validation and local error check. A numerical example demonstrating the feasibility of the surrogate modeling for the limit capacity of the transmission tower under winds is presented. Finally, a fragility assessment concerning a practical transmission line and towers subjected to typhoons is accomplished using the established limit capacity model of the tower.

Keywords: electric transmission line tower; wind-resistant capacity; kriging surrogate; fragility



Citation: Cai, Y.; Wan, J. Wind-Resistant Capacity Modeling for Electric Transmission Line Towers Using Kriging Surrogates and Its Application to Structural Fragility. *Appl. Sci.* **2021**, *11*, 4714. <https://doi.org/10.3390/app11114714>

Academic Editor: Teng Wu

Received: 20 April 2021

Accepted: 11 May 2021

Published: 21 May 2021

Publisher's Note: MDPI stays neutral with regard to jurisdictional claims in published maps and institutional affiliations.



Copyright: © 2021 by the authors. Licensee MDPI, Basel, Switzerland. This article is an open access article distributed under the terms and conditions of the Creative Commons Attribution (CC BY) license (<https://creativecommons.org/licenses/by/4.0/>).

1. Introduction

Vulnerability/reliability analysis on power systems under extreme weather is widely of concern for ensuring the power supply in modern societies. Most research focuses on the overall performance of the power supply [1,2], the resilience of the power network, and the enhancement of the power system [3,4]. However, these studies mainly concentrate on electrical issues and the structural problems are usually expressed in terms of an oversimplified model and sometimes even with only one parameter. The overhead transmission line-tower system (a subsystem of the power network) is sensitive to winds, especially extreme ones (e.g., typhoon [5,6] and downburst [7]). The structural safety of transmission line-tower systems under extreme winds ought to be carefully concerned due to the limited mitigation strategies and time-consuming restoration. Transmission towers, as the support structure of transmission line, are the primary component to assure the safety and function of the system. Therefore, studies on the wind-resistant performance and reliability/fragility

of the tower structure are necessary to promote the structural design, optimization, and safety assessment [8–10].

The tower structure fails under strong winds mainly because the wind loading effect on the structure exceeds its resistant capacity. Most failure cases show the buckling damages on the main force-bearing members of the tower body [11–13]. One approach to explore the wind-resistant capacity of the tower is the progressive failure simulation in which the process starting from plastic hinges and ending with buckling failure is considered [13,14]. The generated capacity curve relating the displacement at the top of the tower to the shear force at the bottom of the tower is used to describe the mechanical performance of the tower. Based on the capacity curve, the elastic/linear behavior and elastoplastic/nonlinear behavior of the tower structure are captured. The nonlinear stage is not expected in a normal working state, so the transition point between the linear and nonlinear stages is usually taken as the damage threshold of the tower structure.

Wind-resistant capacity analysis on the tower structure is essential to assess the fragility/reliability of transmission line towers under winds. Yang et al. [15] discussed the effect of the tower–wire interaction and wind fluctuation on the limit capacity of the tower and then analyzed the fragility of transmission towers subjected to winds. Fu et al. [16], considering the combined effect of the wind and rain, generated fragility curves for transmission towers with the stochasticity of loads involved. Fu and Li [17,18] also simulated a series of fragility curves for transmission towers by taking into account the uncertainty of structures and the stochasticity of winds, respectively. These fragility simulations aim to the two-dimensional fragility curves that relate the failure probability of the tower to the magnitude of wind. However, the wind-induced fragility of transmission towers in a line is a multi-parametric issue [19] with the combined effect of the wind field, tower–wire structure, and geo-distribution of transmission line involved. Therefore, the study of wind-resistant capacity modeling of the transmission tower is necessary for improving and subtilizing the fragility assessment and analysis on transmission line towers.

This paper is dedicated to establishing a limit capacity model for the tower, which can be further applied to the multi-parametric fragility assessment of the transmission line/network under winds. Four parts are involved in the following. First, two limit capacity surfaces described by three external parameters (i.e., the wind speed, wind angle of attack, and the horizontal pan of line) and three wind load components (i.e., the transverse and longitudinal wind loads acting directly on the tower, and the wind load transferred from the transmission wires) are proposed respectively. The two capacity surfaces are approximated by quasi-static gradual-loading nonlinear simulations on the finite element model of the tower, and the mechanical behavior and failure of the tower structure under different wind loadings are demonstrated and discussed. Second, limit state functions are yielded with the capacity function term expressed by the two presented capacity surfaces. Considering the existence of structural uncertainties, the capacity function based on the capacity surface is apparently implicit and high-dimensional. Therefore, a kriging-based adaptive modeling framework is established and used to approximate the capacity surface of the tower. In the framework, the performance of the kriging surrogate is improved continuously by adding support points in each loop and the modeling terminates with the validation results converging or being stationary. Third, based on the kriging surrogate of the wind-resistant capacity of the tower, the fragility simulation on tower structures is conducted using the Monte Carlo method, in which the combined effect of the geo-spatial distribution of the transmission line and winds is involved. An application to the safety assessment of a practical transmission line under typhoons demonstrates the feasibility of the capacity-surface-based fragility simulation. In the last section, the work done in the paper is concluded.

2. Tower Capacity

The steel lattice tower considered in the paper comprises a series of steel members which can be classified into main members, diagonal members, and auxiliary members

(Figure 1). The main members and diagonal members are the primary force-bearing members. The main members determine the global stability of the tower and the diagonal members provide the main members with constraints. There are two types of auxiliary members: the diaphragm and secondary bracing, which improve the overall stability of a tower by offering redundant constraints.

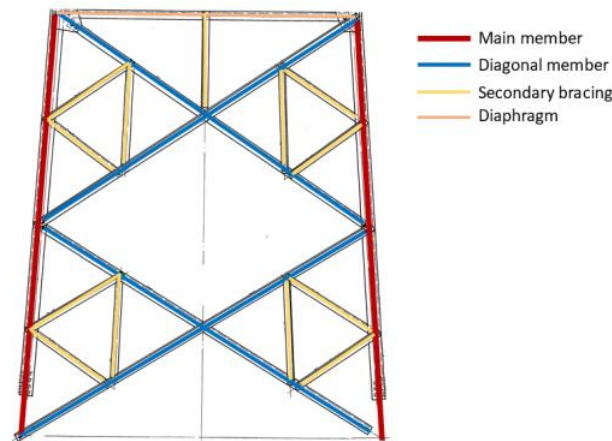


Figure 1. Classification of tower members.

The design function of the steel members is given by DL/T 5154–2012 [17]:

$$\lambda R \geq \gamma_0 \left(\sum \gamma_{Gi} \cdot S_{Gik} + \varepsilon \sum \gamma_{Qj} \cdot S_{Qjk} \right) \quad (1)$$

where λ is the strength factor and R is the nominal strength, γ_0 is an importance factor taken to be 1.0, γ_{Gi} is the dead load factor taken to be 1.0 for tower gravity and 1.2 for the equivalent gravity transferred from transmission wires (including the conductors and ground wires), S_{Gik} is the effect of nominal dead loads on tower members, ε is the weight coefficient of variable loads taken to be 1.0, γ_{Qj} is the variable load factor taken to be 1.4, and S_{Qjk} is the effect of nominal variable loads on tower members.

As the supporting structure, the total design load of transmission towers can be classified into two parts: one is the vertical load, which contains the tower gravity and the equivalent gravity transferred from transmission wires; the other is the horizontal load, which contains the wind load acting on towers directly and the equivalent wind load transferred from transmission wires. Wind loads are the only variable load concerned in this paper and all the tower members are in the elastic state under the action of maximum design wind speed.

2.1. Wind Loading

Wind loads on structures is generally calculated by:

$$F_W = \frac{1}{2} \rho_{air} V^2 \cdot C_D A \quad (2)$$

where ρ_{air} is the density of air, taken to be 1.235 kg/m³, V is the wind speed, C_D is the drag coefficient, and A is the effective area of the wind loading. Here, we set the wind speed V as the 10-min averaged wind speed U at 10 m above the ground. The drag coefficient C_D should jointly take into account the vertical variance of wind speed, the combination effect of the wind fluctuation and structural vibration, and the shape factor of structures. Considering the effect of the wind angle of attack φ (i.e., the intersection angle between the wind direction and the direction transverse to the transmission line), the wind load directly acting on transmission towers is given by [20,21]:

$$H_T = \frac{1}{2} \rho_{air} U^2 \cdot \sum_i \mu_z^i \beta_z^i \left(u_{s,t}^i A_{s,t}^i \cos^2 \phi + u_{s,l}^i A_{s,l}^i \sin^2 \phi \right) \cdot \left[1 + 0.2 \sin^2(2\phi) \right] \quad (3)$$

where i is the section number of the tower, μ_z is a combined wind factor accounting for the altitude and terrain effects, β_z is a gust response factor accounting for the wind fluctuation and structural vibration effects, and $A_{s,t}$ and $A_{s,l}$ and $\mu_{s,t}$ and $\mu_{s,l}$ are the projected areas and shape factors of the transverse and longitudinal faces of the tower, respectively. The term $[1 + 0.2 \sin^2(2\phi)]$ is an amplification factor that related to the wind angle of attack. The wind load H_T is commonly decomposed into the transverse and longitudinal directions of the transmission line:

$$H_t = \frac{1}{2} \rho_{air} U^2 \cdot \sum_i \mu_z^i \beta_z^i \left(u_{s,t}^i A_{s,t}^i \cos^2 \phi + u_{s,l}^i A_{s,l}^i \sin^2 \phi \right) \cdot \left[1 + 0.2 \sin^2(2\phi) \right] \cdot \cos \phi \quad (4)$$

$$H_l = \frac{1}{2} \rho_{air} U^2 \cdot \sum_i \mu_z^i \beta_z^i \left(u_{s,t}^i A_{s,t}^i \cos^2 \phi + u_{s,l}^i A_{s,l}^i \sin^2 \phi \right) \cdot \left[1 + 0.2 \sin^2(2\phi) \right] \cdot \sin \phi \quad (5)$$

where H_t and H_l are the wind load components transverse and longitudinal to the transmission line, respectively. The wind load transferred from transmission wires to the tower structure is given by [20,21]:

$$H_w = \frac{1}{2} \rho_{air} U^2 \cdot \sum_j \mu_z^j \beta_{z,w}^j \mu_{s,w}^j d^j \cdot \sin^2(90^\circ - \phi) \cdot \alpha L_h \quad (6)$$

where j is the number of transmission wires, $\beta_{z,w}$ is the gust response factor of wires, $\mu_{s,w}$ is the shape factor of wires, d is the outer diameter of the wires, L_h is the horizontal span of the transmission line, and α is a span factor accounting for the span-wise non-uniform distribution of wind speed and determined by the wind speed U . The calculations for the above interaction parameters between the wind and tower, and between the wind and transmission wires, are given in the Table A1 in Appendix A.

The wind loading to a transmission tower is composed of three parts: H_t , H_l , and H_w . For a given tower and transmission line, with the terrain type known, there are three independent variables that affect the wind loading to the tower structure, i.e., the wind speed U , the wind angle of attack ϕ , and the horizontal span of transmission line L_h .

2.2. Limit Capacity

Tower structures exhibit nonlinear characteristics when the deformation grows to some extent [14,15]. The capacity curve relating the displacement at the tower top to the shear force at the tower bottom is commonly used to describe the wind-resistant performance of the tower, by which the linear and nonlinear stages can be readily identified [16,22]. The point of transition between the two stages is usually taken as the damage threshold of the tower because the nonlinear behavior is unexpected for the tower structure from the perspective of design and safety. However, a capacity curve can only show the performance of the tower under a single loading case. In reality, the wind loading to a tower is determined by the tower itself as well as transmission wires; it is jointly related to the wind intensity and the wind direction and it is influenced both by the wind field and by the spatial configuration of the transmission line. Hence, this paper uses the capacity surface instead of the capacity curves to describe the wind-resistance capacity of the tower.

2.2.1. Capacity Surface

According to Equations (4)–(6), the wind load on a transmission tower can be decomposed into three components, the transverse wind load acting on the tower (i.e., H_t), the longitudinal wind load acting on the tower (i.e., H_l) and the wind load transferred from transmission wires (i.e., H_w). Taking the three components as the principal axes, the limit capacity of the tower under winds can be described by the surface shown in Figure 2a. Correspondingly, the limit capacity of the tower can be expressed by a function in the form

of Equation (7). Connecting the origin to the capacity point on the surface, we get the vector \mathbf{H}_C , whose direction and magnitude represent one load combination/ratio of three components and the load-carrying capacity of the tower under the combination, respectively. It is noteworthy that the three wind load components are not fully independent and they are influenced by some mutual parameters. In the real case, the capacity surface is usually not a complete surface, as Figure 2a shows, but a partial region. If the information of the tower structure and the line is given, there are three independent parameters determining the wind loading to the tower, i.e., the wind speed U , the wind angle of attack ϕ (here, we ignore the correlation between the wind speed and wind direction), and the horizontal span of the line L_h . Therefore, the limit capacity of the tower can also be described by the capacity surface with the three independent parameters as the principal axes (Figure 2b) and the corresponding limit capacity function is written as Equation (8). One point on the surface means the limit wind speed that the tower can sustain under the certain wind angle of attack and horizontal span. Here, the two capacity surfaces are named surface θ_H , which is expressed by three wind load components, and the surface θ_L , which is expressed by three independent external parameters. It is noteworthy that as the principal axes of the surface θ_L are independent of each other, the region for the surface is explicit and determined by the ranges of U , ϕ , and L_h .

$$f_1(H_t, H_l, H_w) = 0 \quad (7)$$

$$f_2(U, \phi, L_h) = 0 \quad (8)$$

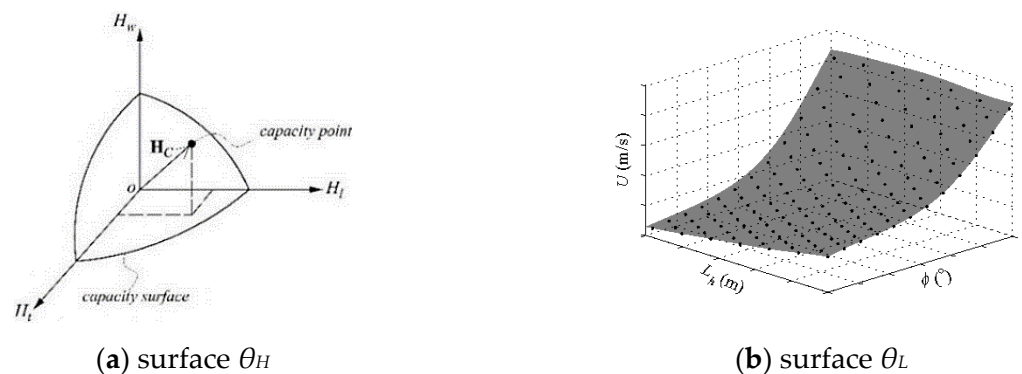


Figure 2. Capacity surfaces of transmission towers.

2.2.2. Example

Here, we take a practical transmission line and the typical transmission tower in the line as the example, and generate the capacity surfaces for the typical transmission tower by numerical simulations. There are 109 towers in the example line with total length of 31.12 km. The typical transmission tower named tower ZY, as the suspension tower [19], accounts for more than 80% of the towers in the line. Table 1 shows the design information of tower ZY, transmission wires, and the line.

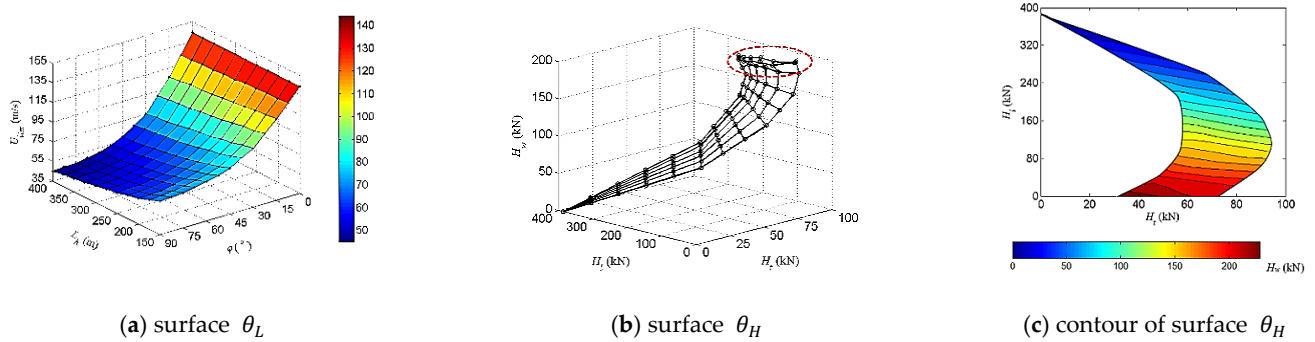


Figure 4. Capacity surfaces of tower ZY.

2.2.3. Discussion

The surface θ_L , shown in Figure 4a, can be fitted effectively by a cubic polynomial:

$$U_{lim} = a_{00} + a_{10}\phi + a_{01}L_h + a_{20}\phi^2 + a_{11}\phi L_h + a_{02}L_h^2 + a_{30}\phi^3 + a_{21}\phi^2 L_h + a_{12}\phi L_h^2 \quad (9)$$

From Equation (9), we see that the limit of the wind speed that the tower structure can sustain has a second-power relation with the horizontal span and a third-power relation with the wind angle of attack. Compared with the horizontal span, the wind angle of attack has more intensive influence in the limit capacity of the tower under winds.

From Figure 4b,c, the region of surface θ_H is a gradual-changing partial band. The tendency of surface θ_H approaches to a linear plane, but the non-linear tendency becomes obvious with the proportion of the wind load transferred from transmission wires (i.e., H_w) increasing. The simulation results (see Appendix B) show that the structure fails in a brittle way if the wind load components H_t and H_l are dominant, while the tower structure fails in a ductile way if the wind load component H_w is dominant. Appendix B gives the capacity curves and failure modes of tower ZY under different combinations of three wind load components (Figure A1 in Appendix B). From the failures of tower ZY (Figure A2 in Appendix B), we can further see the damages of the tower are different under different combinations of three wind load components: the buckling damage occurs at the panel over tower legs when the sum of H_t and H_l accounts for the dominate proportion; the buckling damage occurs at the middle of the tower body when H_w accounts for the dominate proportion.

Surface θ_L and surface θ_H show the limit of the wind-resistant capacity of tower from the perspectives of the wind speed and wind load, respectively. Accordingly, the limit state function of the transmission tower under winds can be written as:

$$g_1 = -f_1(U, \phi, L_h; \theta_S) = U_{lim}(\phi, L_h; \theta_S) - U \quad (10)$$

$$g_2 = -f_2(H_t, H_l, H_w; \theta_S) \quad (11)$$

The limit state function, as the primary function for fragility analysis, consists of a capacity function and a demand function. Surface θ_L expresses a capacity function with the limit wind speed U_{lim} dependent on the wind angle of attack and horizontal span of transmission line. Surface θ_H gives a capacity function in terms of three wind load components. The two capacity surfaces are high-dimensional especially when the structural parameters (presented by the vector θ_S) involve uncertainties. Concerning the structural fragility of towers in a transmission line subjected to winds, the following study focuses on solving the capacity function that expressed by surface θ_L (as well as by surface θ_H) using surrogate models instead of high-fidelity models (e.g., finite element simulations).

3. Kriging-Based Adaptive Surrogate Modeling for Limit Capacity of the Tower

We use ψ to represent the capacity function; then, ψ can be taken as the function of limit wind speed and written as Equation (12) according to the surface θ_L :

$$U_{\text{lim}} = \psi(\phi, L_h; \theta_S) \quad (12)$$

The wind angle of attack and horizontal span are taken as the external variables, and partial structural parameters are taken as the uncertainties. Thus, the capacity function ψ is a multi-dimensional probabilistic problem. In order to clarify the capacity function, numerous loading cases and simulations are required. Instead, we adopt the kriging method [23] in the study and establish an adaptive model to approximate ψ in a more efficient way. Compared with the classical methods (e.g., Taylor-expansion-based methods), kriging is more flexible when it is applied to the surrogate modeling, which allows it to construct an empirical surrogate error measure that can be propagated to the final quantity of interest.

3.1. Kriging Method

The kriging method assumes that the target function relating the input (vector \mathbf{x}) to the output (vector \mathbf{y}) is a sample path of a Gaussian process whose mean and auto-covariance functions are determined by observation points $\mathbf{X} = [\mathbf{x}^1 \dots \mathbf{x}^p]^T$ and the corresponding observation results $\mathbf{Y} = [\mathbf{y}^1 \dots \mathbf{y}^p]^T$ (p is the number of observations) [24]. The observation result \mathbf{Y} is usually solved by high-fidelity simulations or experiments, and can be viewed as the true solutions for the input observation point set \mathbf{X} . The observation set $\mathbf{Y}(\mathbf{X})$ is named as the design of experiment (DoE) and the set $[\mathbf{X} \ \mathbf{Y}]$ is also called the experiment set. The kriging method constructs a Gaussian process based on the DoE, and then predicts the output y corresponding to an arbitrary input x . The Gaussian process for the approximation of a target function can be written as:

$$\mathbf{y}(\mathbf{x}) = \mathbf{f}(\mathbf{x})^T \boldsymbol{\beta} + z(\mathbf{x}) \quad (13)$$

where $\mathbf{f}(\mathbf{x})$ is a functional set used for regression, $\boldsymbol{\beta}$ is the regression coefficient vector, and $z(\mathbf{x})$ is a zero-mean stationary Gaussian process with the variance σ_y^2 and correlation function R . A kriging model involves three steps [25,26]: (i) generating the observation points $\mathbf{X} = [\mathbf{x}^1 \dots \mathbf{x}^p]^T$ and results $\mathbf{Y} = [\mathbf{y}^1 \dots \mathbf{y}^p]^T$; (ii) selecting the kriging functions, i.e., the regression functional set $\mathbf{f}(\mathbf{x})$ and the correlation function R ; (iii) producing the kriging prediction model. Here, the Latin-hypercube sampling are used to generate the initial observation points \mathbf{X} , and the observation results \mathbf{Y} are solved based on finite element simulations. The regression functional set $\mathbf{f}(\mathbf{x})$ and correlation function R are selected as:

$$\mathbf{f}(\mathbf{x}) = [1 \quad x_1 \quad x_2 \quad \dots \quad x_n] \quad (14)$$

$$R(\mathbf{x}^j, \mathbf{x}^k) = \prod_i^n \exp\left(-\theta_i |x_i^j - x_i^k|^2\right) \quad (15)$$

where x_i ($i = 1, 2, \dots, n$) is the element of the input vector \mathbf{x} , n is the number of input variables that contained in the vector \mathbf{x} , $j, k = 1, \dots, p$, and θ_i is the correlation function parameter which is optimized using the principle of maximum likelihood estimation (MLE) [24]. Then, the mean and error variance of the kriging prediction in terms of a new input vector \mathbf{x} are, respectively, expressed as [23]:

$$\hat{\mathbf{y}}(\mathbf{x}) = \mathbf{f}(\mathbf{x})^T \hat{\boldsymbol{\beta}} + \mathbf{r}(\mathbf{x})^T \mathbf{R}^{-1}(\mathbf{Y} - \mathbf{F}\hat{\boldsymbol{\beta}}) \quad (16)$$

$$\sigma_{\hat{\mathbf{y}}}^2 = \sigma_y^2 \left[1 + \mathbf{u}(\mathbf{x})^T (\mathbf{F}^T \mathbf{R}^{-1} \mathbf{F})^{-1} \mathbf{u}(\mathbf{x}) - \mathbf{r}(\mathbf{x})^T \mathbf{R}^{-1} \mathbf{r}(\mathbf{x}) \right] \quad (17)$$

where $\hat{\beta} = (\mathbf{F}^T \mathbf{R}^{-1} \mathbf{F})^{-1} \mathbf{F}^T \mathbf{R}^{-1} \mathbf{Y}$ is the predicted value for β , which is determined by the observation of $\mathbf{Y}(\mathbf{X})$. $\mathbf{F} = [\mathbf{f}(\mathbf{x}^1) \dots \mathbf{f}(\mathbf{x}^p)]^T$, $\mathbf{R} = \{R(\mathbf{x}^j, \mathbf{x}^k)\}$. $\mathbf{r}(\mathbf{x}) = [R(\mathbf{x}, \mathbf{x}^1) \dots R(\mathbf{x}, \mathbf{x}^p)]^T$ indicates the correlation between the observation input points \mathbf{x} and the new input \mathbf{x} . $\mathbf{u}(\mathbf{x}) = \mathbf{F}^T \mathbf{R}^{-1} \mathbf{r}(\mathbf{x}) - \mathbf{f}(\mathbf{x})$; $\sigma_y^2 = (\mathbf{Y} - \mathbf{F} \hat{\beta})^T \mathbf{R}^{-1} (\mathbf{Y} - \mathbf{F} \hat{\beta}) / p$.

The above kriging prediction is fundamentally an interpolation process whose fitting quality depends on the experiment set (i.e., DoE). The interpolation process considers the tendency of the target function and the random correlations of points in the region of concern simultaneously. The kriging model yields a mean value for the predicted output as well as a prediction error variance, which is helpful to measure the accuracy of surrogate modeling.

3.2. An Adaptive Modeling Framework

Based on the kriging method, we propose a kriging-based adaptive surrogate modeling framework (Figure 5) in which three main parts are involved, i.e., the kriging model, support points, and model validation. In the framework, the performance of the kriging surrogate is improved continuously by adding support points in loops. The common approach for selecting the support point is sequential, that is, just one support point (i.e., the point at which the prediction error is largest) is chosen in each loop [24]. To be more efficient, we try to identify a larger sample set of support points in each loop. In this strategy, the points at which the performance of the kriging surrogate is lower have a larger probability of being selected as support points. Concerning the overall accuracy of the surrogate model, an additional issue should be considered, namely, that the selected support points may be close to one another, which can lead to a redundant effect on surrogate performance improvements. To be more effective, the optimization of the support point set is necessary in each loop. At the end of each loop, the accuracy of the kriging model and the validation of the surrogate should be examined, based on which we can decide if we continue the next loop or not. Overall, in this framework, three issues are of major concern: (i) selecting support points (i.e., to generate the initial support point set in an efficient way); (ii) optimizing the support point set (i.e., to remove the inclusion of support points that are close to one another); (iii) validating the surrogate model (i.e., determining whether to terminate the loop or not).

From Equations (16) and (17), the kriging prediction gives both the mean value $\hat{y}(\mathbf{x})$ and the error variance σ_y^2 . The error variance reveals the accuracy of the predicted mean value. Here, we take the prediction error variance as the measure for the selection of support points. That is, more support points should be selected from the regions where the error variance is larger. This means that the larger the prediction error variance is, the more likely the point is to be selected as the support point. Therefore, the original sample set of support points should satisfy a probability distribution whose density monotonically increases with the prediction error variance. To this end, the reject sampling technique is used [27] to generate the initial set of support points. Then, the clustering method is used to eliminate the inclusion of support points that close to one another. Considering that the k-means method is easy to trap in local optimum [28], the bisecting k-means method [29] combined with the iterative self-organizing data technique algorithm (ISODATA) is used to implement the optimization. The steps for generating the support point set in each loop are listed as:

- (i). Generate the original sample set of support points X^* (with the scale of n^*) using the reject sampling technique.
- (ii). Divide the original support point set into K clusters using the bisecting k-means method.
- (iii). Set the lower limit of distance between two nearby clusters as d_{min} ; set the lower limit of number of clusters as $N_{s,min}$; set the upper limit of standard deviation of each cluster as $Sigma$; set the largest number of iterations as N_{iter} ; denote the number of clusters as N_c (the initial value is K).

(iv). Calculate the scale of each cluster and the standard deviation of the samples in each cluster.

(v). Find the clusters whose standard deviations are larger than σ and whose scales are two times larger than $n_{s,min}$; split the cluster into two new clusters with their two center points located at $\pm\sigma$ to the original center point.

(vi). Calculate the distance between any two of the clusters; find the two clusters between which the distance is less than d_{min} and merge them afterwards (only one merging is allowable for each cluster).

(vii). If $N_c < K/2$, turn to step (iv); if $N_c > 2K$, turn to step (vi); if the number of iterations reaches N_{iter} or the iteration approaches to convergence, move to step (viii).

(viii) Gather the center points of the clusters and take these center points as the optimized support point set X^{**} .

Taking the support point set X^{**} as the input, we get the corresponding output Y^{**} through high-fidelity simulations or experiments. Then, add $Z^{**} = [X^{**} Y^{**}]$ to the experiment set and the updated DoE can then be used to construct a new kriging model with the higher performance.

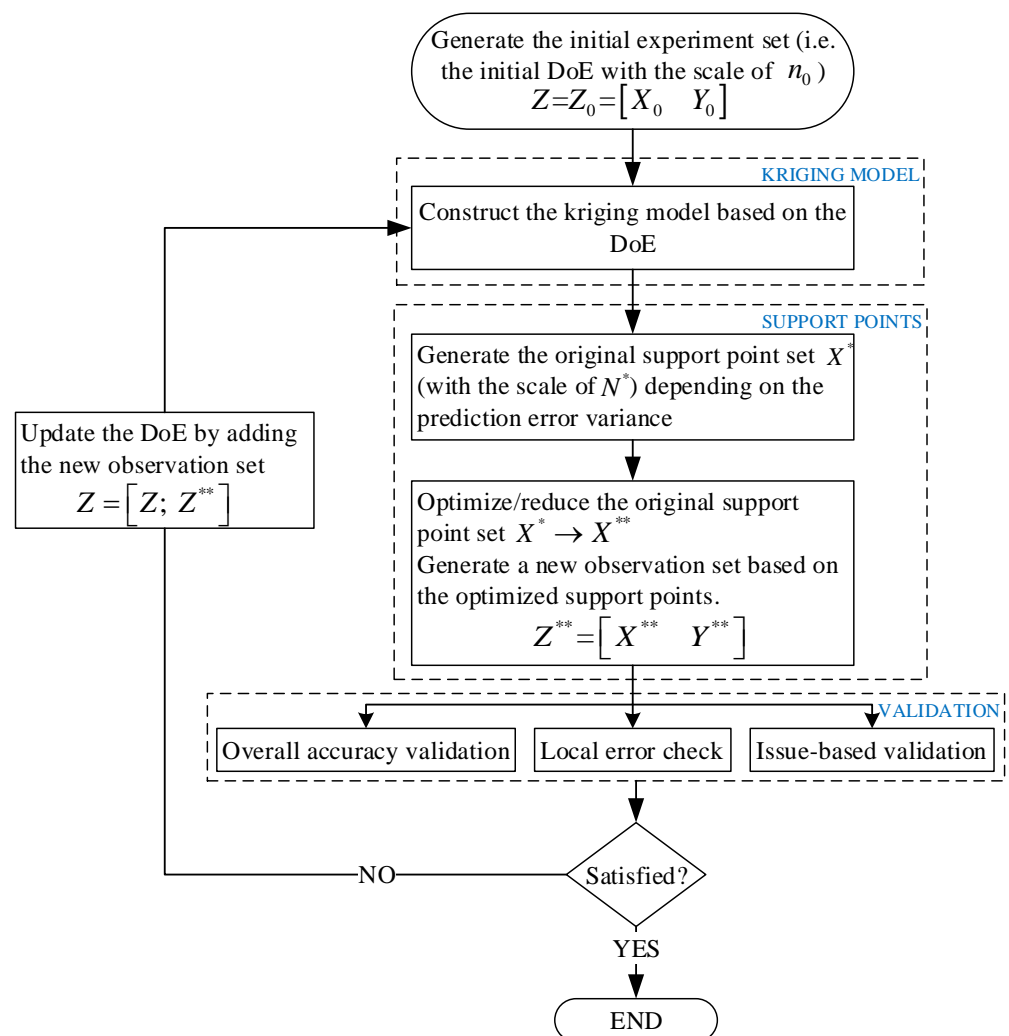


Figure 5. Kriging-based adaptive surrogate modeling framework.

There are two tasks in the model validation. One is to judge if the loop terminates or not. The other is to check the effectiveness of the kriging surrogate. To this end, three parts are included in the validation. First, considering the overall accuracy of the kriging model, a cross-validation method [30] is adopted. The cross validation divides the experiment

set (i.e., DoE) into two groups. One group is used to construct the kriging model and the other is used as the validation set. Based on the error measures, the accuracy of model is evaluated depending on the two groups. Instead of establishing an independent validation set, the cross-validation technique is more efficient and feasible. Here, we utilize the random sampling for the cross validation: (i) sample n points from the experiment set (scale N) that are taken as the validation set, and the residual $(N-n)$ points are used to construct the kriging model; (ii) predict the output for validation points using the constructed kriging model and measure the prediction errors; (iii) repeat the sampling, prediction, and error measuring; (iv) calculate the statistical error. To assure the reliability of cross validation, the sample scale n should be small enough and the number of repeats should be large enough. Therefore, we set $n = 1$ with N being the number of repeats. The coefficient of determination (RD, Equation (18)), accounting for the overall accuracy of the prediction, and the mean error percent (ME, Equation (19)), accounting for the overall deviation of the prediction, are used as the statistical error measures. The larger DR and smaller AME implies better overall performance of the kriging model.

$$RD_i^2 = 1 - \frac{SSE}{SST} \quad (18)$$

$$ME_i = \frac{\sum_{p=1}^N |y_i(\mathbf{x}^p) - \hat{y}_i(\mathbf{x}^p)|}{\sum_{p=1}^N |y_i(\mathbf{x}^p)|} \quad (19)$$

where i means the i -th element of output vector \mathbf{y} , y represents the observation result (i.e., true value), \hat{y} is the prediction of y (i.e., estimated value), \mathbf{x} is the sampled validation point, the upper index p means the p -th repeat, and n is the total number of repeats.

Second, considering the local error of the kriging model, we take the support point set generated in the loop as another validation set for local validation. The roots of the mean square error (RMSE, Equation (20)) and mean absolute error (MAE, Equation (21)) are used to measure the local performance of the kriging model:

$$RMSE = \sqrt{\frac{1}{m} \sum_{j=1}^m (\hat{y}_j - y_j)^2} \quad (20)$$

$$MAE = \frac{1}{m} \sum_{j=1}^m |\hat{y}_j - y_j| \quad (21)$$

where m is the number of validation points (i.e., the scale of the support point set in each loop). The scale of the support point set is generally small and insufficient to check the overall accuracy of the kriging model. Most points in the support point set have a larger prediction error variance, which is helpful to validate the local performance of the kriging surrogate.

Third, the kriging method, as a mathematical approach, does not reveal the nature of the engineering or physical issues. Therefore, it is necessary to validate the performance of the surrogate in engineering practice. In this study, the surrogate for the wind-resistant capacity surface of transmission towers is of concern. In the surrogate, a Gaussian process is used to approximate the points on the capacity surface, and these capacity points are characterized by probabilities. In other words, instead of a single surface, the surrogate model aims at a group of surfaces that characterized by probabilities. The details of the issue-based validation are demonstrated in the following example study.

3.3. Example Study

In the example study, the capacity function ψ in Equation (12) is the target function we need to approximate using kriging models. Function ψ is an implicit function dependent on the external variables (i.e., the wind angle of attack φ and horizontal span of line L_H) and structural parameters of transmission line towers (i.e., θ_S). The structural vector θ_S

contains the information of material, geometry, the initial state, and boundary conditions. Uncertainties in these structural parameters may lead to the uncertainty in the wind-resistant capacity of the tower. In general, the boundary condition of tower legs was taken as rigid, and the initial state and damping ratio of the tower structure had neglectable influences on the limit capacity of the tower [31]. Hence, we did not take into account the uncertainties of the boundary condition, initial state, and structural damping ratio in this case. Thus, the material and geometry are the two primary uncertainties concerned in the study.

Taking the practical transmission tower ZY in Figure 3 as an example, the probabilistic features of structural parameters are listed in Table 2.

Table 2. Probabilistic features of structural parameters.

Material [32]	Mean (μ)	C.O.V (δ)	Distribution
Yield strength ($f_{y,Q345}$)	387 MPa	0.07	Lognormal
Yield strength ($f_{y,Q235}$)	264 MPa	0.07	Lognormal
Elastic modulus (E_s)	206,000 MPa	0.03	Lognormal
Poisson ratio (ν)	0.3	0.03	Lognormal
Geometry [17]	Mean */standard deviation (μ/σ)	C.O.V (δ)	Distribution
Thickness of angle steel members (t)	0.985	0.032	Normal
Length of angle steel members (l)	1.001	0.008	Normal

* The mean value of geometrical parameters is determined by the design size.

Two types of steel with different yield strengths ($f_{y,Q345}$ and $f_{y,Q235}$) were used in the tower structure. The two external variables (i.e., the wind angle of attack φ and horizontal span of line L_h in Equation (12)) were taken as normal variables with their values distributing uniformly in their ranges. According to the transmission line information shown in Table 1, the range of φ is 0° – 90° and that of L_h is set to 150–400 m. In the kriging modeling, the wind angle of attack φ , the horizontal span L_h , and structural parameters θ_S are the input of the model, i.e., $\mathbf{x} = [\varphi \ L_h \ \theta_S]$. The structural vector θ_S contains six random parameters, i.e., $\theta_S = [f_{y,Q345}, f_{y,Q235}, E_s, \nu, t, l]$. The logarithm of limit wind speed $\ln U_{lim}$ was taken as the output of the model, i.e., $\mathbf{y} = \ln(U_{lim})$.

Following the above framework, we first generated the initial DoE $[X_0 \ Y_0]$ using the Latin hypercube sampling technique. The scale of the initial experiment set is taken to be $n_0 = 100$. Based on the initial DoE, we constructed the initial kriging model by adopting the first-order polynomial regression function set (shown as Equation (14)) and Gaussian's correlation function (shown as Equation (15)). Then, we moved to the second stage, i.e., generating the support point set. The scale for the initial set of support points was taken to be $n^* = 1000$. During the optimization process, the expected scale for the support point set was taken to be 100 (i.e., the initial number of clusters $K = 100$). The final scale for the support point set in each loop ranged from 50 to 200.

At the validation stage, we first calculated the overall accuracy measures (shown as Equations (18) and (19)) of the kriging model. Then, we took the optimized support point set as the local validation set and calculate the local error measures (shown as Equations (20) and (21)). Figure 6 gives the trends of the accuracy/error measures with the loop number increasing.

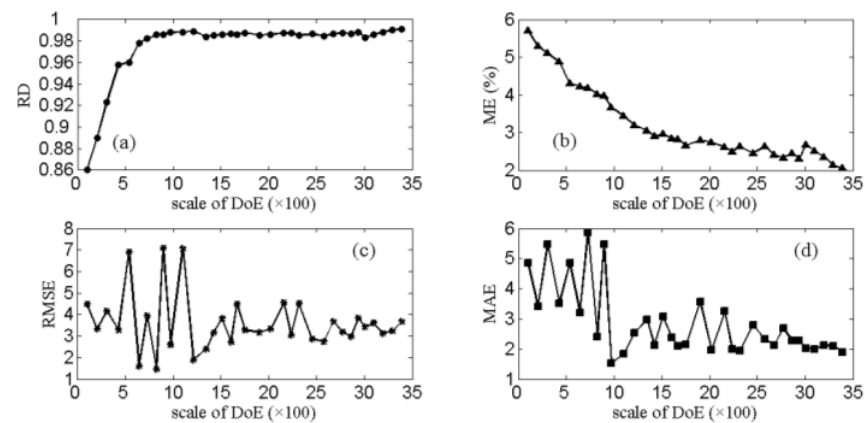


Figure 6. Accuracy/error measures of the kriging model. (a) the change of RD; (b) the change of ME; (c) the change of RMSE; (d) the change of MAE.

As can be seen in Figure 6a, the coefficient of determination (RD) grew quickly to a value of 0.98 and then kept stable. The mean error percent (ME) continuously decreased with the scale of DoE increasing. When the value of ME reached 2%, we terminated the adaptive modeling. Then, the modeling process ended when the number of points used to construct the kriging model was close to 3500. Concerning the local performance of the kriging surrogate, Figure 6c,d show the trends of the local error measures RMSE and MAE. In this process, RMSE fluctuated around the value of 3.5 and the fluctuation weakened with the scale of DoE increasing. MAE shows a decreasing trend with the final value approximating to 2, and the fluctuation of MAE became less obvious in the latter process.

Figure 7 further gives the comparison result between the kriging prediction and the observation result in the last loop of the adaptive modeling. Most of the predicted values were located in the range of $\pm 5\%$ error, and the prediction yielded satisfactory results when the limit wind speed was less than 100 m/s.

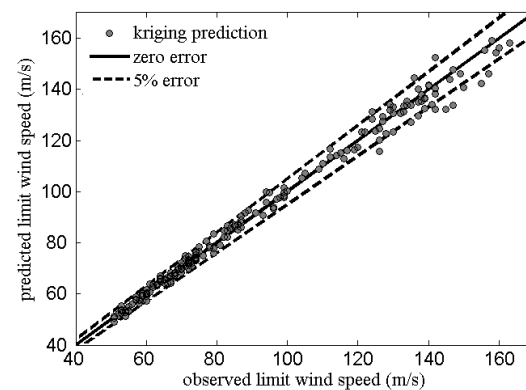


Figure 7. The comparison between the predicted result and the observation result.

The kriging model is expected to predict an assembly of capacity surfaces for transmission towers that subjected to winds, and these capacity surfaces are characterized by probabilities. The prediction on limit wind speed aims at a probability distribution rather than a single value. Hence, in the region of interest, the kriging prediction is the prediction of an assembly of probability distributions. At the issued-based validation step, we first generated 10,000 samples randomly, depending on probabilistic features of structural parameters (shown in Table 2). The 10,000 samples were taken as the set of prediction points, which was characterized by randomness. Then, we took 42 points of the capacity surface uniformly based on the ranges of the wind angle of attack and horizontal span, and the 42 surface points were taken as the set of validation points. In each loop, the constructed kriging model was used to predict the limit wind speed at each validation

point of the capacity surface and 10,000 samples of the tower were involved in each validation point. Then, the mean value and standard deviation of the limit wind speed at each validation point were calculated, which further yielded the change ratio of the mean value and standard deviation (Equations (22) and (23)) with the loop number increasing:

$$R_{\mu}^{i,j} = \frac{|\mu_i^j - \mu_{i-1}^j|}{\mu_{i-1}^j} \tag{22}$$

$$R_{\sigma}^{i,j} = \frac{|\sigma_i^j - \sigma_{i-1}^j|}{\sigma_{i-1}^j} \tag{23}$$

where μ_i^j and σ_i^j are the mean and standard deviation of the limit wind speed of the j -th validation point in the i -th loop. Taking 42 validation points into account, the averages of $R_{\mu}^{i,j}$ and $R_{\sigma}^{i,j}$ (with $j = 1, 2, 3 \dots 42$) and the maximums of $R_{\mu}^{i,j}$ and $R_{\sigma}^{i,j}$ in each loop were derived to evaluate the performance of the kriging surrogate. Figure 8 shows the trends of the averages and maximums of change ratios with the scale of DoE increasing.

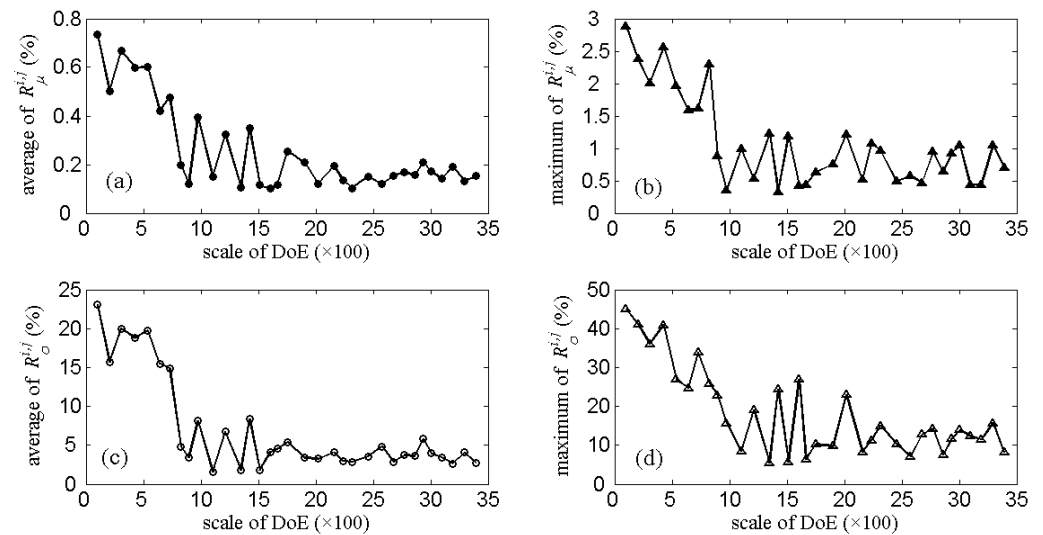


Figure 8. Averages and maximums of change ratios. (a) the average change ratio of the mean; (b) the max change ratio of the mean; (c) the average change ratio of the standard deviation; (d) the max change ratio of the standard deviation.

As can be seen in Figure 8a, the average change ratio of the means of 42 validation points decreased with the increasing scale of DoE, and when the scale reached 2000, this measure fluctuated slightly around 0.2%. Similarly, the average change ratio of the standard deviations of 42 validation points (Figure 8c) reduced and kept fluctuating around 5% with the scale getting to 2000. Comparatively, fluctuations of the maximum of change ratios are more apparent (Figure 8b,d).

According to the above validation results (Figures 6–8), the presented adaptive kriging modeling for capacity surface θ_L of transmission towers is feasible and effective. Figure 9a shows the surrogate result for capacity surface θ_L of tower ZY using the proposed adaptive modeling framework. Correspondingly, the approximated capacity surface θ_H is shown in Figure 9b according to the wind loading relations (i.e., Equations (4)–(6)).

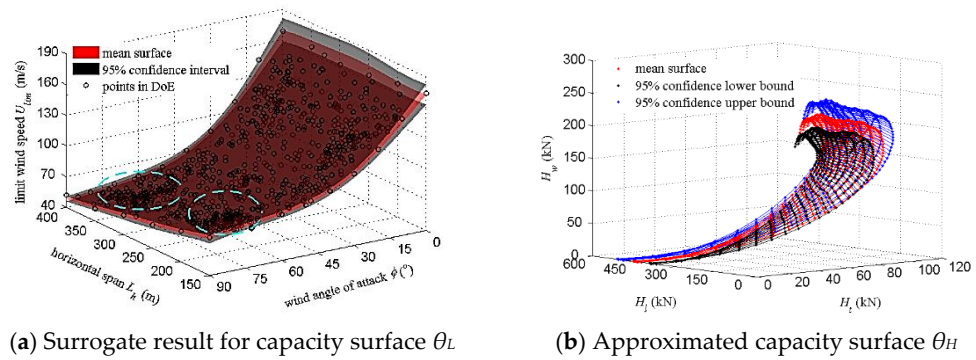


Figure 9. The surrogate result for capacity surfaces.

In Figure 9a, most of the support points are in the two regions enclosed by green curves, which indicates that the limit capacity of the tower is more sensitive to the structural uncertainty in these two regions. Comparing Figure 9b with Figure 4b, it is shown that the trends of capacity surface θ_H are similar. With the load component H_w increasing, the surfaces exhibit a more significant nonlinear trend.

4. Application to the Structural Fragility Assessment on a Transmission Line

The above study constructed a capacity function for the limit state of transmission towers subjected to winds, and solved the capacity function by the proposed kriging-based surrogate modeling. Considering the capacity surface θ_L , the limit state function is written as:

$$g = U_{lim} - U = \psi(\phi, L_h; \theta_S) - U \tag{24}$$

where ϕ and L_h are the normal variables; θ_S is a structural vector containing stochastic structural parameters. Based on the above limit state function, the fragility curves can be simulated through the workflow shown in Figure 10 (Θ_S is the sample assembly of the stochastic structural vector θ_S ; N_s is the scale of Monte Carlo sampling; $N(g < 0)$ means that the number of elements that less than zero in the limit state vector \mathbf{g}).

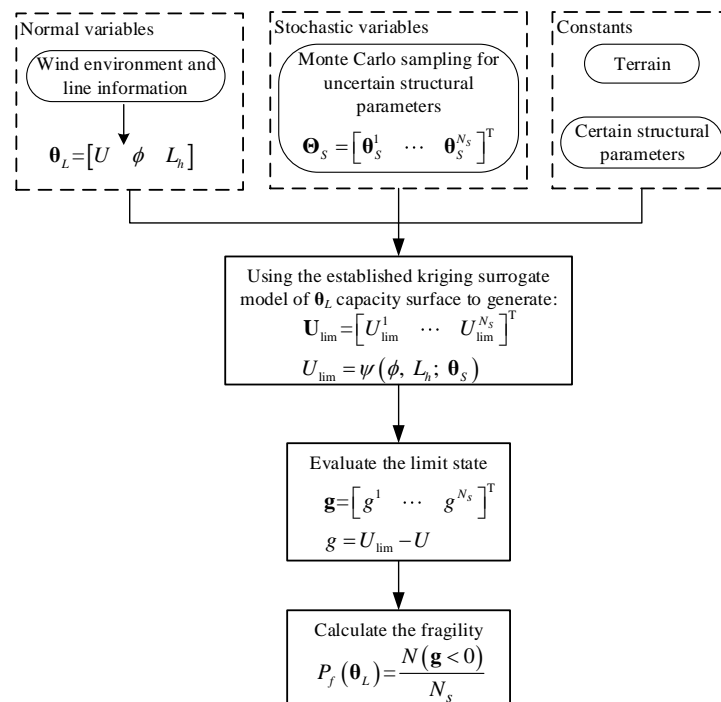


Figure 10. The flow for generating the structural fragility of towers under winds.

Depending on the established kriging surrogate model of capacity surface θ_L , we can generate multiple groups of fragility curves for the transmission tower with its structural uncertainties considered and the external variables (i.e., the wind environment and line span) involved. Figure 11 further gives the fragility curves of tower ZY achieved by the above flow, in which different wind angles of attack and three horizontal spans are of concern.

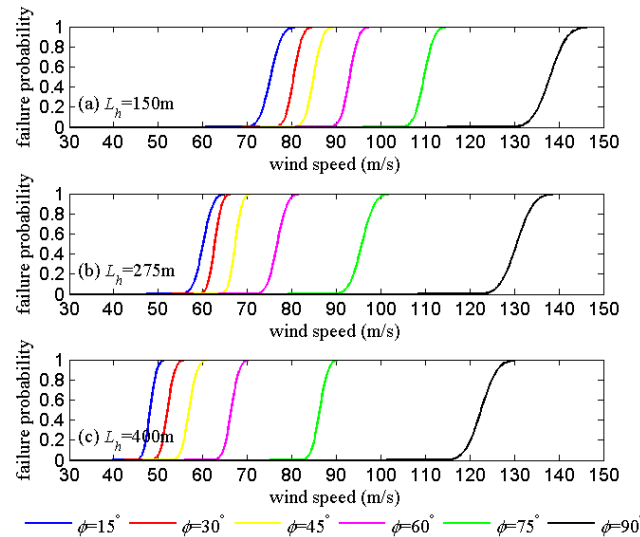


Figure 11. Structural fragility curves of tower ZY. (a) $L_h = 150$ m; (b) $L_h = 275$ m; (c) $L_h = 400$ m.

Taking the practical transmission line (Table 1) as the example and considering the normal segment of the line (i.e., the blue section in Figure 12), we conducted the structural fragility assessment on the towers and the line segment under typhoons by implementing the workflow of the fragility calculation, shown in Figure 10.

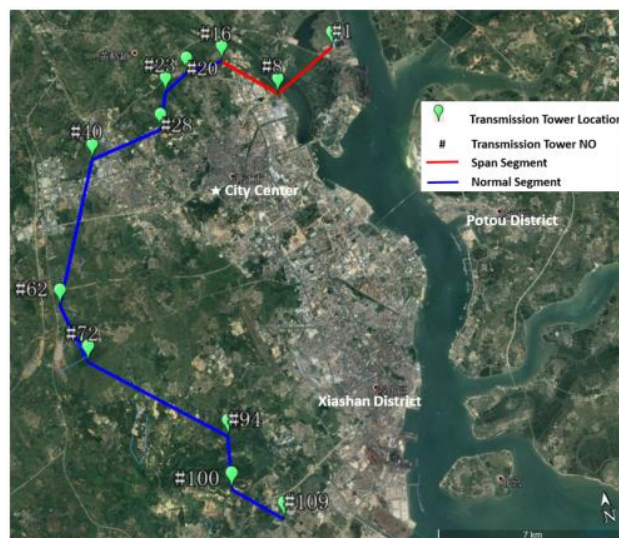


Figure 12. A practical transmission line. * The background image is captured from Google Earth Pro [33].

In the normal segment of the line, there were 86 transmission towers in total, including 71 suspension tangent towers, 14 tension towers, and 1 terminate tower. Suspension tangent towers, as the wind-sensitive structure, are concerned in the fragility assessment. Tension towers and terminate towers generally have a higher safety level under winds and are not considered here. Taking the wind and the line information into account simultaneously, the

annual probability of failure of each tower can be estimated by convolving the structural fragility with the joint model of the annual extreme wind speed of typhoons (v) and the corresponding wind direction (β) as:

$$P_{f,T} = \int_0^{360} \int_0^{v_{\max}} F_T(v, \phi | L_h, \alpha) f_{v,\beta}(v, \beta) dv d\beta \quad (25)$$

in which $P_{f,T}$ is the annual probability of failure of the tower structure and F_T represents the cumulative probability of failure of the tower with the horizontal span and line direction taken as L_h and α , respectively. This cumulative probability is a function of the annual extreme wind speed of typhoons v and the corresponding wind angle of attack ϕ (ϕ is calculated according to the line direction α and the direction of annual extreme wind β), which can be calculated using the workflow shown in Figure 10. $f_{v,\beta}$ is the joint probability density of the annual extreme wind speed (v) and its wind direction (β), in which the wind speed v and direction β range from $0-v_{\max}$ and $0^\circ-360^\circ$, respectively. Here, we adopt the joint probability model of v and β that are generated based on the 60-year typhoon on-site data (Figure 13) [34–36]. This joint model is established by combining the Monte Carlo simulation with the two-dimensional non-parametric kernel density estimation [37]:

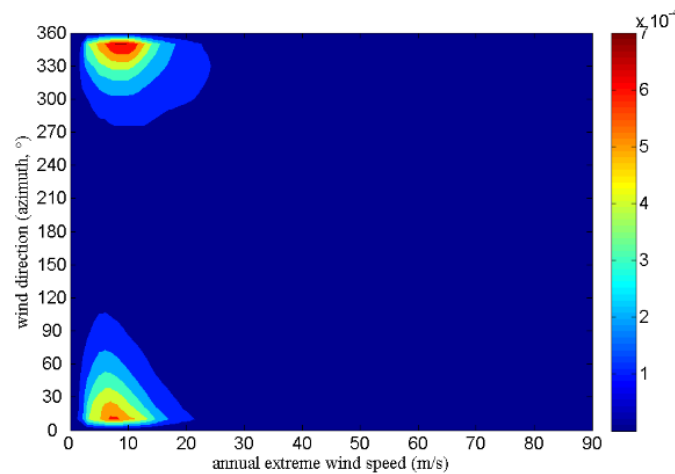


Figure 13. Joint probability model of the annual extreme wind speed of typhoons and the wind direction.

Then, we obtain the annual probability of failure of each suspension tower in the normal segment of the transmission line using Equation (25), and the failure probabilities of tension towers and terminate towers are taken to be zero. Clustering the suspension towers based on the line direction and span, we obtain three clusters of the towers, with their centers corresponding to different line directions (Figure 14a). In Figure 14a, n denotes the number of the towers located in the corresponding cluster. Figure 14b further shows the failure class of each tower in three clusters. The failure class is defined by the annual probability of failure calculated from the Equation (25) and five classes are classified according to the calculation result. In Figure 14a,b, the red cluster accounts for the majority of the towers and their failure probabilities scatter in the five classes. Considering the blue cluster and the black cluster, we find that most of the towers have larger failure probabilities.

Defining one strain section of a line as starting from one tension tower and ending with the adjacent tension/terminate tower, there are 14 strain sections in the normal segment of the transmission line. To evaluate each strain section, Figure 15a,b first give the basic information (including the length and the number of the towers) of each strain section, and we have the essential cognition that the longer the strain section is, the more towers are included in the section. Figure 15c,d further show the statistical result of the annual failure probability of the towers in each strain section.

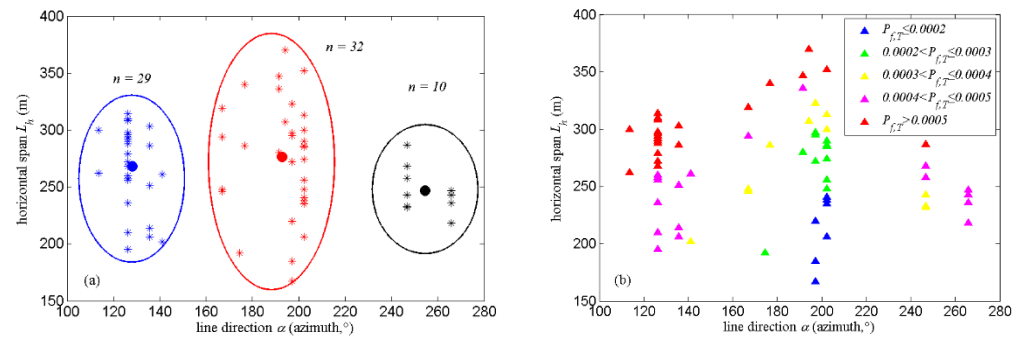


Figure 14. Clusters of suspension towers and their failure classes. (a) clusters of suspension towers; (b) failure classes of suspension towers.

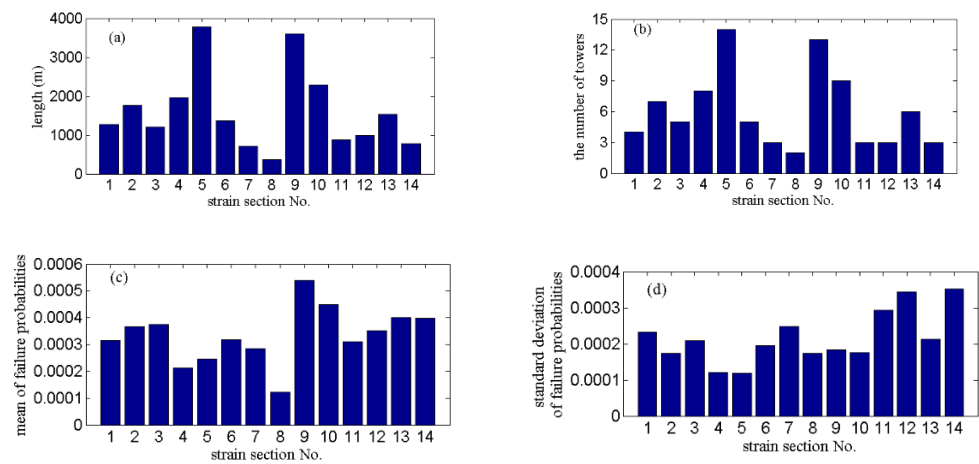


Figure 15. Strain sections and the annual failure probability of towers in each strain section. (a) the length of each strain section; (b) the number of towers in each strain section; (c) the mean of failure probabilities of each strain section; (d) the standard deviation of failure probabilities of each strain section.

Comparing the two strain sections with the largest numbers of towers, i.e., section No. 5 and No. 9, we found that although the No. 5 section owns the largest number of towers, its annual failure risk is quite low in terms of both the average and deviation. No. 9 section has the highest failure risk from the perspective of average, while No. 12 and 14 sections have the larger deviations. Furthermore, we considered the failure of stain sections using the bound theory (shown as Equations (26) and (27)):

$$\text{Lower bound } P_{f,L} \geq \max [P_{f,T}(T_j)] \tag{26}$$

$$\text{Upper bound } P_{f,L} \leq 1 - \prod_j^m [1 - P_{f,T}(T_j)] \tag{27}$$

where $P_{f,L}$ is the annual probability of failure of one strain section or line segment, $P_{f,T}(T_j)$ represents the annual probability of failure of the j -th tower, $j = 1, 2, \dots, m$, and m is the total number of towers in the strain section. Using the Equations (26) and (27), we obtained the failure bounds of each strain section, as shown in Figure 16.

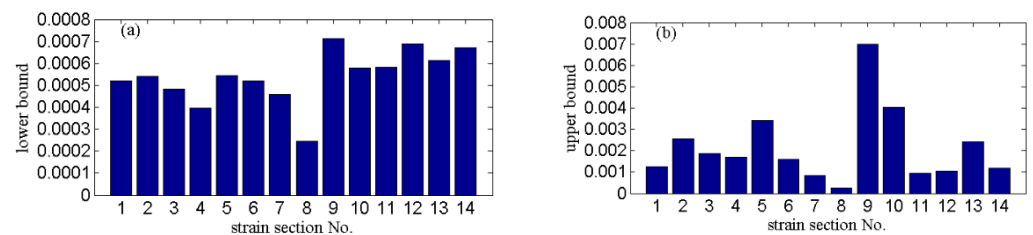


Figure 16. Failure bounds of each strain section. (a) the lower bound of failure probabilities; (b) the upper bound of failure probabilities.

In Figure 16, the No. 9 section has the highest lower bound as well as the highest upper bound among all the strain sections, which indicates that the most dangerous tower is in the No. 9 strain section and most of the towers in this section have a higher risk. Moreover, the lower bounds of No. 10–No. 14 sections are also considerably high, which means that there are also dangerous towers located in these sections.

Based on the above assessment, we conclude the following (from the perspective of annual failure risk):

- (i). The primary attention should be drawn on the No. 9 strain section due to its high risk of failure.
- (ii). The No. 5 strain section, owning the largest number of the towers, shows a relatively low failure risk.
- (iii). Considering the whole normal segment, the first part of the segment (i.e., No. 1–8 strain sections) exhibits a lower failure risk than the latter part of the segment (i.e., No. 9–14 strain sections), which indicates that the latter part of the normal segment is of greater significance for assuring the annual safety of the line that subjected to typhoons.

5. Conclusions

The fragility/vulnerability assessment of transmission tower structures subjected to winds is a multi-parametric issue. To this end, the paper proposes the surface expression (i.e., the surfaces θ_L and θ_H) for the wind-resistant capacity of the tower, based on the wind loading rule. The limit capacity of a certain tower is described by a function related to three external parameters, as well as by a function related to three wind load components, after which the corresponding limit state functions of tower structures can be obtained. In order to acquire the capacity surfaces, the explicit algorithm-based non-linear static simulation is applied to the finite element model of the tower and a series of wind loading cases are involved. The simulation results yield the fitted/approximated capacity surfaces of an example tower by taking the transition point of capacity curves as the damage threshold.

Applying the capacity surface θ_L to the limit state function of the tower structure under winds, the capacity function term is constructed. Considering the structural fragility, the capacity function is high-dimensional and characterized by the stochasticity. For solving the high-dimensional probabilistic relation, a kriging-based adaptive modeling framework is established to approximate the capacity function. The constructed kriging model is expected to predict the points on the capacity surface θ_L , and these capacity points are characterized by stochasticity. Therefore, rather than a single surface, the kriging surrogate aims to approximate an assembly of surfaces.

In the proposed modeling framework, the performance of the kriging surrogate is improved by adding support points. Three steps (i.e., the generation of support points, the optimization of the support point set, and the model validation) are involved to assure the effectiveness of the adaptive modeling. In the example study, the validation results (including the overall accuracy validation, the local error check and the practical issue-based validation) demonstrate the feasibility of the framework with all of the accuracy/error measures approaching to convergence/stationarity after a sufficient number of loops.

By applying the established kriging surrogate of the capacity surface, a group of structural fragility curves for transmission towers are obtained, in which geo-spatial information of the line and wind (i.e., the line direction, the line span and the wind direction) is considered simultaneously. Depending on the fragility model, it is capable to do the fragility assessment on transmission towers and line under winds. Considering the safety of tower structures under typhoons, the annual failure probability of each tower in a practical transmission line is calculated by combining the capacity-surface-based fragility model with the joint probability model of the annual extreme wind speed and wind direction of typhoon. By the failure risk assessment on each strain section of the line, some suggestions are made for evaluating and improving the safety of the transmission line.

Taking the line direction and span, the wind direction, and intensity into account, this paper explores an effective approach to establish and solve the capacity function for transmission towers under winds, and then assess the structural fragility of tower structures and transmission line. To do the fragility analysis more precisely, much more factors are needed to be involved (e.g., the wind stochasticity, the variance of terrain, and the service time of the transmission line). Correspondingly, a higher dimensional model for the wind-resistant capacity of the tower is required.

Author Contributions: Conceptualization, Y.C.; methodology, Y.C.; software, Y.C.; validation, J.W.; formal analysis, J.W.; investigation, Y.C.; resources, Y.C.; data curation, Y.C.; writing—original draft preparation, Y.C.; writing—review and editing, J.W.; visualization, J.W. All authors have read and agreed to the published version of the manuscript.

Funding: This research received no external funding.

Institutional Review Board Statement: Not Applicable.

Informed Consent Statement: Not Applicable.

Conflicts of Interest: The authors declare no conflict of interest.

Appendix A. Interaction between the Wind and the Transmission Line Towers

Four types of interaction parameters are concerned, the combined wind factor (μ_z and $\mu_{z,w}$), accounting for the effect of the altitude and terrain on the wind field, the gust response factor (β_z and $\beta_{z,w}$), accounting for the load effect due to the turbulence of the wind and the dynamic amplification of the tower and wires, the shape factor (μ_s and $\mu_{s,w}$), accounting for the effect of structural members (e.g., the member size, shape and solidity), and the span factor (α), accounting for the reduction effect due to the non-uniform distribution of the wind speed along the line. In this work, these interaction parameters are calculated according to the design codes/specifications (Table A1), referring to the IEC Standard 60826 [21], the ASCE-74 [38], the Chinese load code (GB 50009–2012) [39], and the Chinese code for design of 110 kV–750 kV overhead transmission line (GB 50545–2010) [40]. To determine the interaction parameters, four types of data are necessary: the wind intensity data (e.g., the 10-min averaged wind speed at 10 m over the ground); structural data, including the geometric and mechanical properties of the tower and wires; spatial data, including the direction and span of the line; and terrain data, which affects the altitude-dependent wind distribution and wind turbulence.

Table A1. Wind-structure interaction parameters.

Parameters	Tower Structure	Transmission Wires	Remarks
Combined wind factor [21]	$\mu_z = (z/z_0)^{\alpha_0}$	$\mu_{z,w} = (z/z_0)^{\alpha_0}$	The power law is adopted here. z is the height of concern, z_0 is the reference height taken to be 10 m, and α_0 is the roughness exponent. I_z is the turbulence intensity of winds, B (including B_t and B_w) is the background component of the structural response, L_s is the integral scale of turbulence of winds, z is the height of the tower section, and S is the span of line. A_s and A are the projected area and the area of the outer profile of the tower section, respectively, η is the geometrical factor of the tower section, and d is the outer diameter of the wire. U is the 10-min-averaged wind speed at 10 m over the ground.
Gust response factor [37]	$\beta_z = \left(\frac{1+4.6I_z B_t}{1+6.1I_z} \right)$ $B_t = \sqrt{\frac{1}{1+\frac{0.56z}{L_s}}}$	$\beta_{z,w} = \left(\frac{1+4.6I_z B_w}{1+6.1I_z} \right)$ $B_w = \sqrt{\frac{1}{1+\frac{0.8S}{L_s}}}$	
Shape factor [38]	$\mu_s = \frac{A_s}{A}(1 + \eta)$	If $d < 17$ mm, $\mu_{s,w} = 1.2$ If $d \geq 17$ mm, $\mu_{s,w} = 1.1$	
Span factor [39]	-	$U < 20$ m/s, $\alpha = 1.00$; 20 m/s $\leq U < 27$ m/s, $\alpha = 0.85$; 27 m/s $\leq U < 31.5$ m/s, $\alpha = 0.75$; $U \geq 31.5$ m/s, $\alpha = 0.70$.	

Appendix B. Simulation Results of the Limit Capacity of Transmission Towers under Winds

Considering the ranges of the wind angle of attack (0° – 90°) and horizontal span (100–400 m), we conducted a series of simulations on the finite element model of tower ZY and the capacity curves of tower ZY under different wind loading cases generated by the explicit algorithm-based non-linear static analysis (Figure A1). The capacity curve was drawn by relating the tower top displacement to the wind speed and to the bottom shear force, respectively (see Figure A1a,b). From Figure A1, the mechanical behavior of the tower structure can be divided into two stages: one is the linear/elastic stage and the other is the nonlinear/plastic stage. The transition of the two stages is defined as the damage threshold of the structure. The wind speed magnitude that corresponds to the transition point was taken as the limit wind speed that the tower can sustain. Figure A1 further notes the proportions of three wind load components (i.e., H_t , H_l , and H_w) at the limit/transition point of the capacity curves. From Figure A1, we have the plastic stage gets shorter with the proportion of the sum of H_t and H_l increasing. Figure A2 further shows the failure modes of tower ZY under different combinations/ratios of three wind load components.

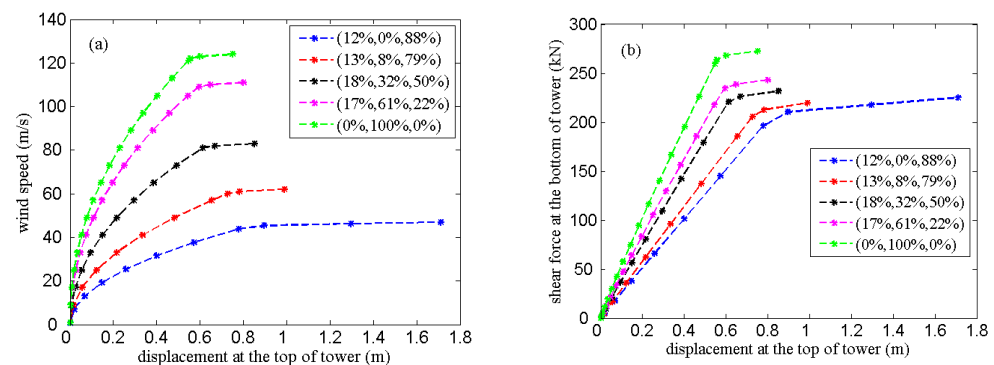


Figure A1. Capacity curves of tower ZY under different wind loading cases. (a) the curve relating the displacement to the wind speed; (b) the curve relating the displacement to the bottom shear force.

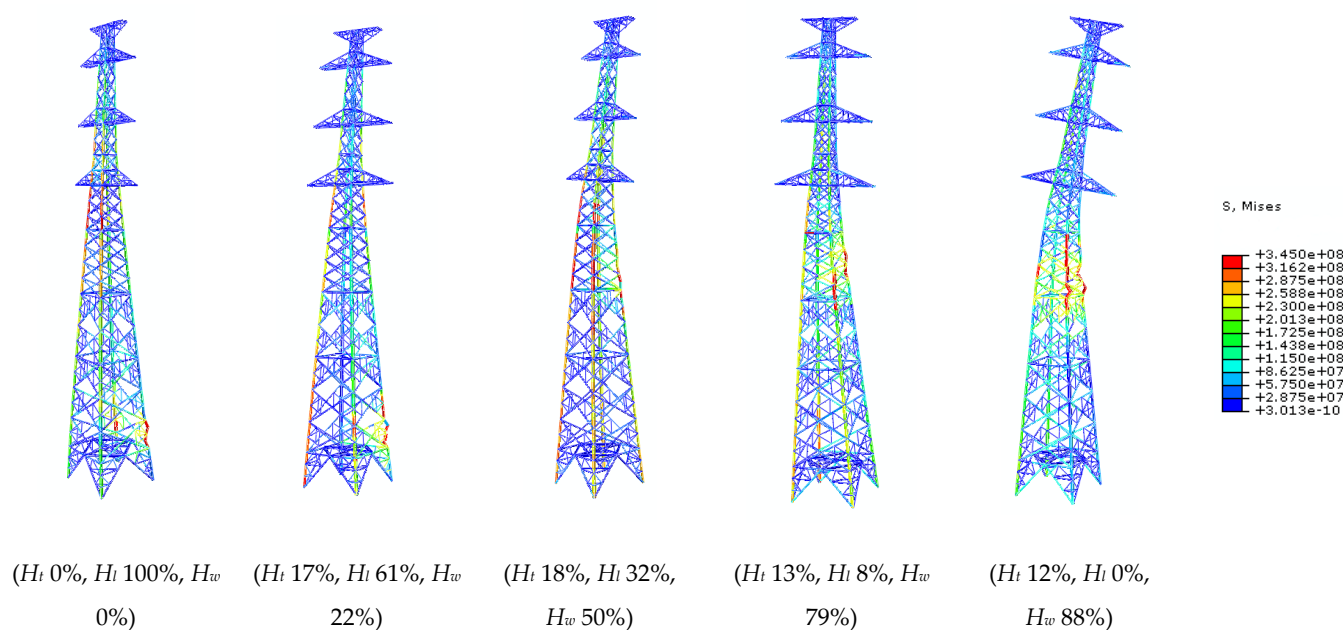


Figure A2. Failures of tower ZY under different combination ratios of three wind load components.

References

- Liu, Y.; Singh, C. Reliability evaluation of composite power systems using Markov cut-set method. *IEEE Trans. Power Syst.* **2010**, *25*, 777–785. [\[CrossRef\]](#)
- Vaiman, M.; Bell, K.; Chen, Y.; Chowdhury, B.; Dobson, I.; Hines, P.; Zhang, P. Risk assessment of cascading outages: Methodologies and challenges. *IEEE Trans. Power Syst.* **2012**, *27*, 631–641. [\[CrossRef\]](#)
- Panteli, M.; Mancarella, P. Influence of extreme weather and climate change on the resilience of power systems: Impacts and possible mitigation strategies. *Elect. Power Syst. Res.* **2015**, *127*, 259–270. [\[CrossRef\]](#)
- Panteli, M.; Pickering, C.; Wilkinson, S.; Dawson, R.; Mancarella, P. Power system resilience to extreme weather: Fragility modelling, probabilistic impact assessment, and adaptation measures. *IEEE Trans. Power Syst.* **2017**, *32*, 3747–3757. [\[CrossRef\]](#)
- Tao, T.; Shi, P.; Wang, H. Spectral modelling of typhoon winds considering nexus between longitudinal and lateral components. *Renew. Energy* **2020**, *162*, 2019–2030. [\[CrossRef\]](#)
- Tao, T.; Wang, H. Modelling of longitudinal evolutionary power spectral density of typhoon winds considering high-frequency subrange. *J. Wind Eng. Ind. Aerod.* **2019**, *193*, 103957. [\[CrossRef\]](#)
- Tao, T.; Shi, P.; Wang, H. Short-term prediction of downburst winds: A double-step modification enhanced approach. *J. Wind Eng. Ind. Aerod.* **2021**, *211*, 104561. [\[CrossRef\]](#)
- Alam, M.J.; Santhakumar, A.R. System reliability analysis of transmission line towers. *Comput. Struct.* **1994**, *53*, 343–350. [\[CrossRef\]](#)
- Natarajan, K.; Santhakumar, A. Reliability-based optimization of transmission line towers. *Comput. Struct.* **1995**, *55*, 387–403. [\[CrossRef\]](#)
- Fenton, G.A.; Sutherland, N. Reliability-based transmission line design. *IEEE Trans. Power Deliv.* **2011**, *26*, 596–606. [\[CrossRef\]](#)
- Prasad, R.N.; Knight, G.M.S.; Mohan, S.J.; Lakshmanan, N. Studies on failure of transmission line towers in testing. *Eng. Struct.* **2012**, *35*, 55–70. [\[CrossRef\]](#)
- Qiang, X.; Li, S. Experimental study on the mechanical behavior and failure mechanism of a latticed steel transmission tower. *J. Struct. Eng.* **2013**, *139*, 1009–1018.
- Tapia-Hernández, E.; Ibarra-González, S.; De-León-Escobedo, D. Collapse mechanism of power towers under wind loading. *Struct. Infrastruct. Eng.* **2017**, *13*, 766–782. [\[CrossRef\]](#)
- Albermani, F.; Kitipornchai, S.; Chan, R.W.K. Failure analysis of transmission towers. *Eng. Fail. Anal.* **2009**, *16*, 1922–1928. [\[CrossRef\]](#)
- Yang, S.C.; Hong, H.P. Nonlinear inelastic responses of transmission tower-line system under downburst wind. *Eng. Struct.* **2016**, *123*, 490–500. [\[CrossRef\]](#)
- Fu, X.; Li, H.N.; Li, G. Fragility analysis and estimation of collapse status for transmission tower subjected to wind and rain loads. *Struct. Safety* **2016**, *58*, 1–10. [\[CrossRef\]](#)
- Fu, X.; Li, H.N. Uncertainty analysis of the strength capacity and failure path for a transmission tower under a wind load. *J. Wind Eng. Ind. Aerod.* **2018**, *173*, 147–155. [\[CrossRef\]](#)

18. Fu, X.; Li, H.N.; Tian, L.; Wang, J.; Cheng, H. Fragility analysis of transmission line subjected to wind loading. *J. Perform. Constr. Fac.* **2019**, *33*, 04019044. [[CrossRef](#)]
19. Cai, Y.Z.; Xie, Q.; Xue, S.T.; Hu, L.; Kareem, A. Fragility Modelling Framework for Transmission Line Towers under Winds. *Eng. Struct.* **2019**, *191*, 686–697. [[CrossRef](#)]
20. DL/T 5154-2012. *Technical Code for the Design of Tower and Pole Structures of Overhead Transmission Line (Industrial Standard)*; Electric Power Planning & Engineering Institute: Beijing, China, 2012.
21. IEC 60826. *Design Criteria of Overhead Transmission Lines*, 3rd ed.; International Electro-technical Commission: Geneva, Switzerland, 2003.
22. Mara, T.G.; Hong, H.P. Effect of wind direction on the response and capacity surface of a transmission tower. *Eng. Struct.* **2013**, *57*, 493–501. [[CrossRef](#)]
23. Sacks, J.; Welch, W.J.; Mitchell, T.J.; Wynn, H.P. Design and analysis of computer experiments. *Stat. Sci.* **1989**, *4*, 409–435. [[CrossRef](#)]
24. Dubourg, V.; Sudret, B.; Bourinet, J.M. Reliability-based design optimization using kriging surrogates and subset simulation. *Struct. Multidisc. Optim.* **2011**, *44*, 673–690. [[CrossRef](#)]
25. Irfan, K. Application of kriging method to structural reliability problems. *Struct. Safety* **2005**, *27*, 133–151.
26. Ioannis, G.; Alexandros, A.T.; George, P.M. Kriging metamodeling in seismic risk assessment based on stochastic ground motion models. *Earthq. Eng. Struct. Dyn.* **2015**, *44*, 2377–2399.
27. Robert, C.P.; Casella, G. *Monte Carlo Statistical Methods*, 2nd ed.; Springer: New York, NY, USA, 2004.
28. Hartigan, J.A.; Wong, M.A. Algorithm AS 136: A K-means clustering algorithm. *J. R. Stat. Soc. C* **1979**, *28*, 100–108. [[CrossRef](#)]
29. Kovaleva, E.V.; Mirkin, B.G. Bisecting k-means and 1D projection divisive clustering: A unified framework and experimental comparison. *J. Classif.* **2015**, *32*, 414–442. [[CrossRef](#)]
30. Meckesheimer, M.; Booker, A.J.; Barton, R.R.; Simpson, T.W. Computationally inexpensive metamodel assessment strategies. *AIAA J.* **2002**, *40*, 2053–2060. [[CrossRef](#)]
31. Takeuchi, M.; Maeda, J.; Ishida, N. Aerodynamic damping properties of two transmission towers estimated by combining several identification methods. *J. Wind Eng. Ind. Aerod.* **2010**, *98*, 872–880. [[CrossRef](#)]
32. JCSS. Probabilistic Model Code—Part 3-Material Properties. JCSS. 2001. Available online: <https://www.jcss-lc.org/jcss-probabilistic-model-code/> (accessed on 1 January 2021).
33. Google Earth Pro V7.3.3.7786. Zhanjiang, Guangzhou Province, China. 21°16'13" N 110°21'33" E, Eye alt 45 km. Available online: <https://www.google.com/earth/> (accessed on 10 September 2017).
34. Ying, M.; Zhang, W.; Yu, H.; Lu, X.; Feng, J.; Fan, Y.; Zhu, Y.; Chen, D. An overview of the China Meteorological Administration tropical cyclone database. *J. Atmos. Ocean Technol.* **2014**, *31*, 287–301. [[CrossRef](#)]
35. Lu, X.Q.; Yu, H.; Yang, X.M.; Li, X.F. Estimating Tropical Cyclone Size in the Northwestern Pacific from Geostationary Satellite Infrared Images. *Remote Sens.* **2017**, *9*, 728. [[CrossRef](#)]
36. Cai, Y.Z. Typhoon Fragility for Electric Transmission Line Based on the Failure of Transmission Towers. Ph.D. Thesis, Tongji University, Shanghai, China, 2019.
37. Bowman, A.W.; Azzalini, A. *Applied Smoothing Techniques for Data Analysis*; Oxford University Press: New York, NY, USA, 1997.
38. ASCE. *Guidelines for Electrical Transmission Line Structural Loading*, 3rd ed.; ASCE Manuals and Reports on Engineering Practice No. 74; ASCE: Reston, VA, USA, 2010.
39. GB 50009-2012. *Load Code for the Design of Building Structures (National Standard)*; Ministry of Construction of the People's Republic of China: Beijing, China, 2012.
40. GB 50545-2010. *Code for Design of 110 kV~750 kV Overhead Transmission Line (National Standard)*; China Electricity Council: Beijing, China, 2010.